JOURNAL OF SOLID STATE CHEMISTRY **137,** 311–324 (1998)
ARTICLE NO. SC977745

Mosaic Crystals of Vanadyl Pyrophosphate Obtained by Oriented Nucleation and Growth

N. Duvauchelle,* E. Kesteman,* F. Oudet,† and E. Bordes*,[1]

*Département de Génie Chimique, and †Service d'Analyse Physicochimique, Université de Technologie de Compiègne, B.P. 20529, F-60205 Compiègne Cedex, France

Received July 7, 1997; in revised form December 17, 1997; accepted December 19, 1997

A study of the pseudomorphic transformation of the $VOHPO_4 \cdot 0.5H_2O$ precursor (P/V=1) to $(VO)_2P_2O_7$ catalyst is reported. Attention is paid to the nucleation and growth stages, which are discussed in connection with the concept of topotaxy. The transformation mechanism which accounts for the textural change is established using electron microscopy techniques and X-ray diffraction. The morphology change to a prismatic shape at high temperature, approximately 870°C, is also discussed.

INTRODUCTION

Topotaxy is a very important phenomenon in the field of reactivity of solids. A topotactic reaction can be defined as a transformation in which one crystalline phase is converted into another with a definite and reproducible crystallographic orientation relationship between the two. Such a definition is in agreement with the official definition of topotaxy given by the International Union of Crystallography and carries no implication regarding the transformation mechanism (1). A wide range of reactions can be said topotactic, from reactions with conservation of the three-dimensional structure to reconstructive reactions.

When one wants good control of crystal morphology, as is necessary in the case of structure-sensitive catalytic reactions, finding a precursor which yields the catalyst topotactically provides opportunity. Indeed, the properties of the pseudomorphic catalyst can be controlled in this way. This is the case, for example, in the preparation of transition aluminas from boehmite (2) or of metallic molybdates (3, 4), and also for $(VO)_2P_2O_7$, the well-known catalyst of the selective oxidation of *n*-butane to maleic anhydride (5). Indeed, when the precursor, $VOHPO_4 \cdot 0.5H_2O$, is dehydrated in an inert atmosphere, pseudomorphic crystals of $(VO)_2P_2O_7$ are obtained because of topotaxy (6, 7, 8).

[1] To whom correspondence should be addressed.

By varying the alcohol used as a reflux medium in preparation of the precursor from V_2O_5 and H_3PO_4, it has been shown that primary (plates or thin sheets) and secondary (piles of plates or "roses of sand") particles may be obtained for both precursor and catalyst (9, 10). The morphology has also been shown to influence the reactivity of the particles in an air–butane stream or in noncatalytic reactions. For a while, two "forms" of vanadyl pyrophosphate, γ and β $(VO)_2P_2O_7$, were thought to exist because of their differences of reactivity. Indeed, in oxygen, these samples were reoxidized to γ-$VOPO_4$ and β-$VOPO_4$, respectively (11, 12).

Another point is that, in an air–butane stream, the vanadyl pyrophosphate catalyst is partly oxidized with the formation of V^{5+}, or even transformed into several types of $VOPO_4$ according to the conditions used by the various authors (13, 14). Nguyen *et al.* (15) assumed that the existence of the V^{5+} species is related to stacking faults, while Thompson *et al.* (16) preferred to emphasize the role of polytypes.

Torardi *et al.* (17) have recently noted that the final product is made up of highly oriented vanadyl pyrophosphate microcrystals and that the large contraction of the atomic structure in the direction perpendicular to the basal plane induces cracks and voids within the crystal. The present paper aims at describing the dehydration of $VOHPO_4 \cdot 0.5H_2O$ in terms of oriented nucleation and growth related to the concept of topotaxy, in order to account for the special texture which characterizes $(VO)_2P_2O_7$ catalyst. The morphology change occurring at high temperature will also be discussed.

EXPERIMENTAL

Preparation

a. $VOHPO_4 \cdot 0.5H_2O$ (precursor). When the starting materials are V_2O_5 and H_3PO_4, two distinct preparation routes are mainly reported in the literature: preparation in an aqueous medium with reduction by HCl or other acids,

0022-4596/98 $25.00

and preparation in an organic medium, generally, alcohol (18). Another synthetic route consists of the reduction of the oxovanadium phosphate dihydrate, $VOPO_4 \cdot 2H_2O$, in alcohol (6, 8, 19).

Well-characterized materials are needed for the present purpose. Among the alcohols chosen, we had already noticed (20) that 2-butanol led to the formation of thin plates with definite morphology. Therefore, V_2O_5 (11.8 g) and H_3PO_4 85% (14.9 g) were mixed in 2-butanol (250 ml). After refluxing for 6 h, the light green suspension was separated from the organic solution by filtration and washed several times with the same alcohol (200 ml), and then with acetone (500 ml), to remove organic residue from the solid. The resulting light green solid was dried in an oven at 120°C (15 h).

b. $(VO)_2P_2O_7$ *(catalyst).* One gram of the precursor was calcined in an alumina boat placed in a quartz tube and heated at 5°C/min in a nitrogen flow ($1\,l\,h^{-1}$). Various temperatures and times of calcination were used, yielding samples called Pyro-420, Pyro-750, and Pyro-870 (Table 1).

c. Partially transformed catalyst. A TGA/DTA apparatus was used to control the formation of a material not yet totally dehydrated (Setaram microbalance TG92, N_2 flow). A 20 mg of Sample $VOHPO_4 \cdot 0.5H_2O$ was heated to 420°C (heating rate: 5°C/min) and quenched at room temperature (sample called P420-Q). The loss of weight (7.2%), clearly below the theoretical one (10.46%), confirms the partial transformation of the sample.

Characterization

The precursor sample and the final products after calcination were characterized by powder X-ray diffraction (XRD) and scanning and transmission electron Microscopy (SEM, TEM).

XRD was performed on powders using an INEL CPS 120 (curve detector) and Cu$K\alpha_1$ radiation (0.15406 nm). The Diffrac-At software was used to calculate the full width at half maximum, β_{exp}, for each main Bragg peak. The instrumental broadening β_{inst} was determined by a calibration procedure using a well-crystallized V_2O_5 material. The broadening due to the sample itself, β_{sample}, was calculated by $\beta^2_{sample} = \beta^2_{exp} - \beta^2_{inst}$. The average crystallite size (L_m) and internal strain (ε) data gathered in Table 1 were evaluated satisfactorily using the Williamson–Hall formula (21):

$$\beta_{sample} \cos\theta = 0.94\,\lambda/L_m + 2\varepsilon \sin\theta.$$

TEM observations were made in a JEOL 1200EX microscope, operating at 80 kV to avoid modification of the sample under the beam. Microdiffraction patterns were also obtained to identify each sample. Powder samples were dispersed in CCl_4 by ultrasonic waves and displayed onto a lacey carbon film supported on a copper mesh grid. SEM analysis was carried out using a JEOL 840C microscope to obtain informations on external morphology.

Potentiometric titration was carried out using the method of Niwa and Murakami (22) to estimate the average oxidation number of vanadium.

The specific surface area was estimated by the one-point BET method, using nitrogen gas at 77 K in Quantasorb equipment.

RESULTS

$VOHPO_4 \cdot 0.5H_2O$

The $VOHPO_4 \cdot 0.5H_2O$ phase crystallizes in the orthorhombic system (P_{mmn}) with $a = 7.416$ Å, $b = 9.592$ Å, and $c = 5.689$ Å (23). The XRD pattern of the solid prepared in 2-butanol shows that the expected single phase, $VOHPO_4 \cdot 0.5H_2O$, is well crystallized. No line broadening of the (001) reflection, which could account for stacking plates disorder such as when organic molecules are trapped in between the sheets (24), is observed (Fig. 1). The value of the internal strain, ε, is thus very low (Table 1). The specific surface area is low and amounts to 4 $m^2\ g^{-1}$.

By SEM, the particles of precursor look like very thick bitrapezoidal platelets (Fig. 2). The TEM observation of several non-isolated particles confirms this particular morphology (Fig. 3a). The presence of Bragg extinction contours, as seen in Fig. 3a, indicates that the platelets are often slightly bent, and that their crystalline state is good. The selected area electron diffraction (SAED) pattern of an isolated particle (Fig. 3b) corresponds to a single crystal lying on the (001) plane, as confirmed by the sharpness of the electron diffraction spots. This is also confirmed by the dark field image of the same particle, which is completely illuminated (Fig. 3b).

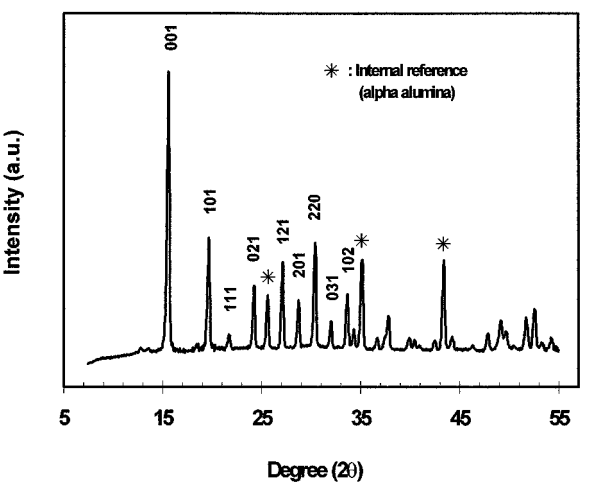

FIG. 1. Powder X-ray diffraction pattern of $VOHPO_4 \cdot 0.5H_2O$ prepared in 2-butanol.

TABLE 1
Characteristics of $VOHPO_4 \cdot 0.5H_2O$ Prepared in 2-Butanol and of the Three Samples of $(VO)_2P_2O_7$ Prepared at Various Temperatures and Times of Calcination

	Temperature of calcination (°C)	Time of calcination (h)	Color	Surface area (m^2/g^{-1})	Oxidation state of vanadium[a]	Average crystallite size[b] Lm (Å)	Internal strain[b] β (* 10^{-3})
Precursor	—	—	Green	4	4	$\gg 1000$	2.35
Pyro-420	420	48	Brown	5.6	4.146	437	9.26
Pyro-750	750	3	Grey	6.1	4.012	995	6.53
Pyro-870	870	24	Blue-grey	1	[c]	$\gg 1000$	4.32

[a] Potentiometric titration (22).
[b] Calculated by the method of Williamson and Hall (21).
[c] Titration could not be performed because of non dissolution of the sample.

These results lead us to conclude that the vanadyl hydrogen phosphate hemihydrate platelets are *monocrystalline monolith* particles, according to the classification proposed by Figlarz *et al.* (25).

$(VO)_2P_2O_7$

The XRD pattern of the samples calcined at various temperatures, characteristic of the $(VO)_2P_2O_7$ phases, has been indexed in the monoclinic system $P2_1$ using the cell parameters given recently by Nguyen *et al.*: $a = 7.7276$ Å, $b = 16.5885$ Å, $c = 9.5796$ Å, $\beta = 89.5796$ (26) (Fig. 4).

The color, the surface area, and the average oxidation state of vanadium vary with the temperature of dehydration (Table 1). Compared with the precursor, a slight increase of the surface areas of Pyro-420 and Pyro-750 is observed. The average oxidation state of vanadium decreases, as observed by Nguyen *et al.* (15), from 4.146 to 4.012.

When compared to the diffraction lines of the $VOHPO_4 \cdot 0.5H_2O$ starting material, a significant broadening is observed for Pyro-420 and Pyro-750 patterns. A weak broadening effect is still noted for Pyro-870. The average crystallite size of Pyro-750 calculated by the method of Williamson-Hall is 995 Å, and the internal strain ε is 6.5×10^{-3}, clearly below that of Pyro-420 (Table 1). However, let us note that the average line $\beta_{\text{sample}} \cos\theta = f(2\sin\theta)$ obtained by the Williamson–Hall method does not fit exactly the experimental points all.

SEM pictures show that the morphology of Pyro-420 and Pyro-750 is different from that of Pyro-870. For Pyro-420 and Pyro-750, the pseudomorphism with precursor is evidenced because platelets with the same bitrapezoidal

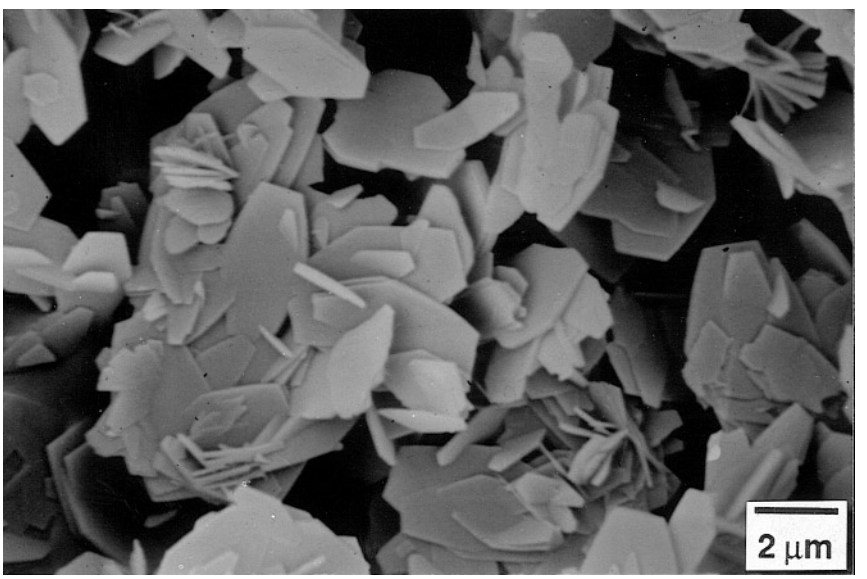

FIG. 2. SEM image of $VOHPO_4 \cdot 0.5H_2O$ prepared in 2-butanol.

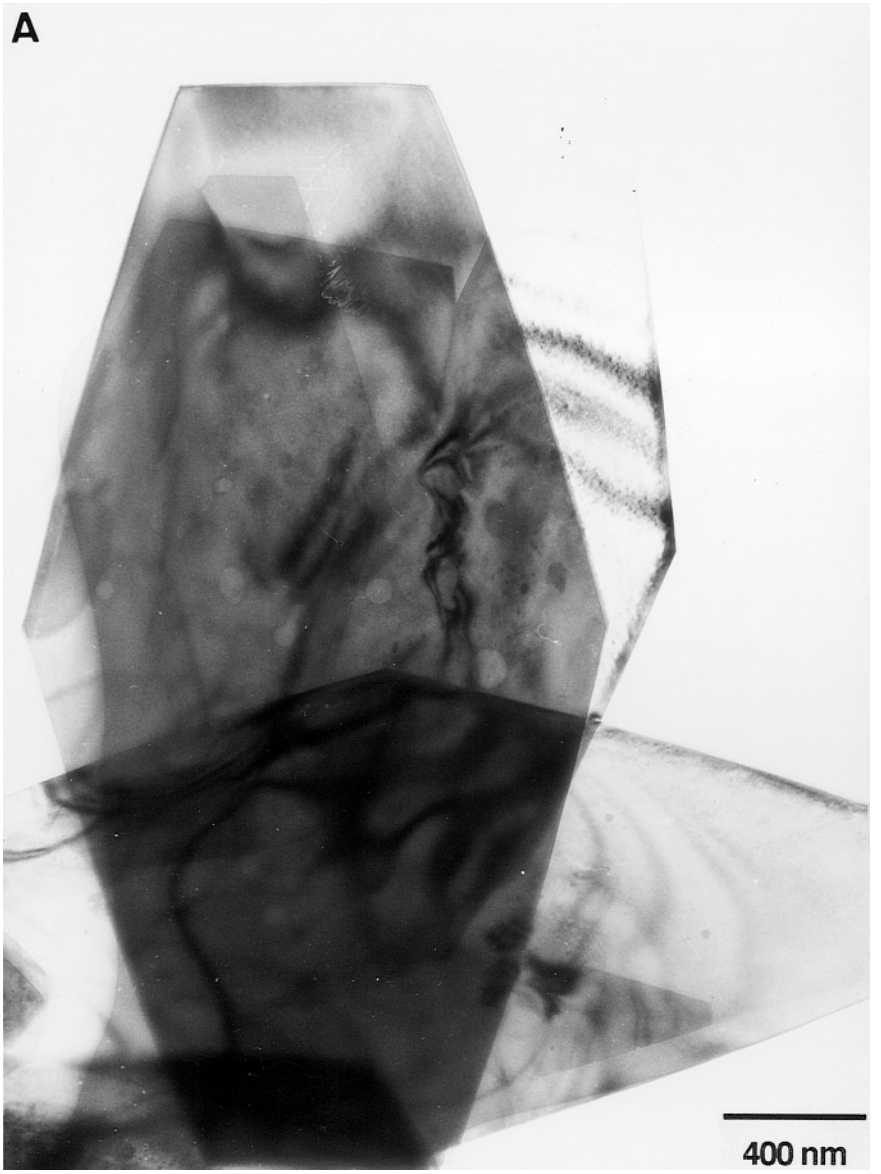

FIG. 3. (a) Bright field image of several particles of $VOHPO_4 \cdot 0.5H_2O$; (b) dark field image of a single precursor particle and corresponding SAED showing the particle lying on the (001) plane.

morphology are observed (Fig. 5a). The surface of each particle is rough and some voids can be seen, especially in the case of Pyro-750. For Pyro-870, the shape and size of the precursor are not retained since particles are prismatic and exhibit a certain degree of sintering between them (Fig. 5b). Because of the size and thickness of the prismatic crystals of Pyro-870, the TEM study could not be made in the same way as for Pyro-420 and Pyro-750.

When examining Pyro-420 and Pyro-750, the first observation by TEM is that platelets are displayed on the (100) plane as shown by SAED, and exhibit the same characteristic shape as the precursor (Figs. 6, 7). SAED and dark field images allow to make some distinctions between them. In the case of Pyro-420, the platelets do not show any Bragg extinction contour and seem to be composed of many microcrystals (i.e., crystallites) (Fig. 6a). Most of the bright regions in the TEM image are due to voids, as suggested by Torardi *et al.* (17), that would explain why the surface area increases a little as compared with the precursor's (Table 1). SAED shows that the diffraction spots are curved, indicating a small misorientation of these crystallites inside the particle (Fig. 6b). Nevertheless, we can consider this sample as made from single crystals lying on the (100) plane. The average crystallite size (437 Å) calculated from XRD by

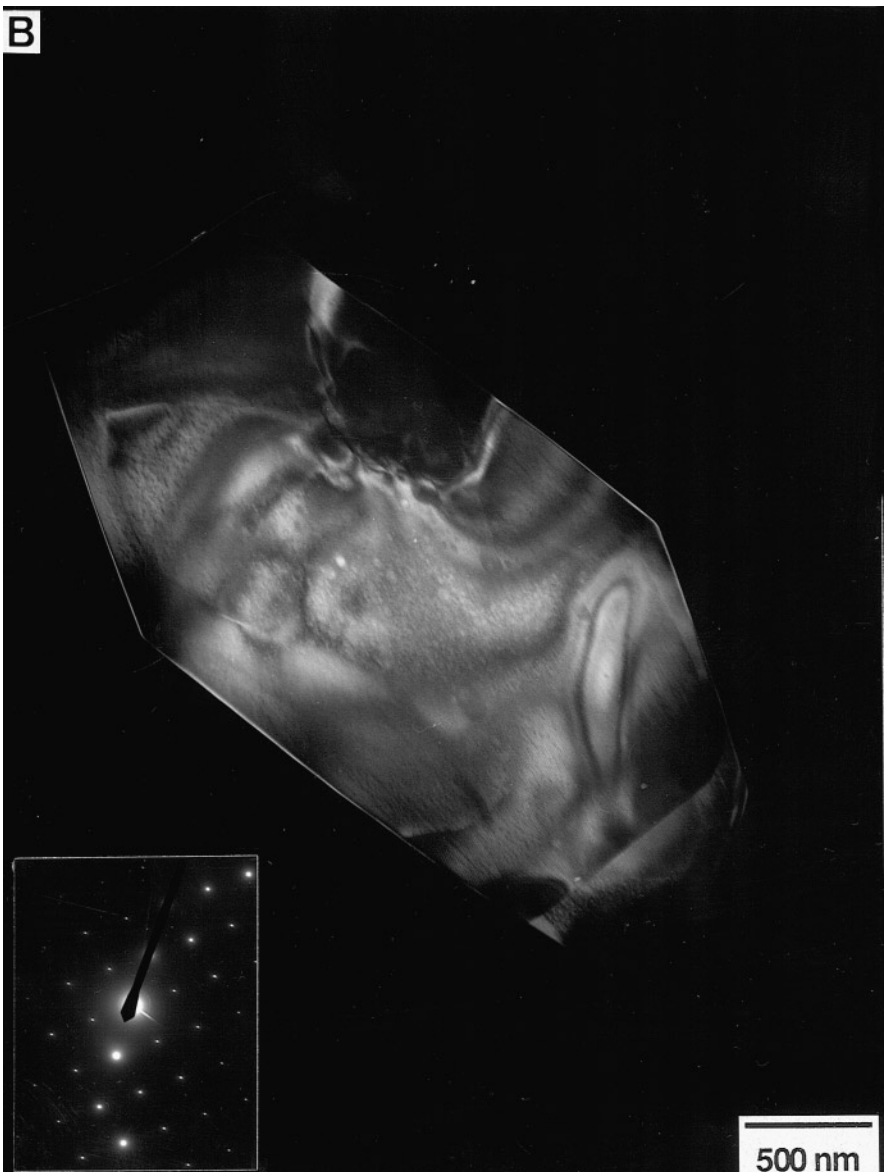

FIG. 3—*Continued*

the Williamson–Hall method, is clearly much smaller than the observed size of the platelets (several micrometers). The dark field image confirms these results more explicitly (Fig. 6b), because only domains in Bragg position in relation to the incident electron beam are observed. These images show a large number of small white spots, the size of which is about the same order of magnitude than the average crystallite size calculated from XRD. Consequently, these white spots "materialize" the crystallites. Finally, the relatively high value ($\varepsilon = 9.2 \times 10^{-3}$) of the internal strain can be related to the presence of small angle boundaries between the crystallites inside the grain. Therefore, we conclude that the Pyro-420 platelets of $(VO)_2P_2O_7$ are *monocrystalline mosaic* particles (25), i.e., they are built up by a great number of small crystallites slightly misoriented with respect to each other.

The microcrystals of Pyro-750 are bigger and exhibit a more "chaotic" aspect, as for the particle shown Fig. 7a. When looking at the center of this particle, some voids are observed, together with a large, individual, crystallite which seems to stand out of the particle. This is confirmed by the dark field image which shows two distinct areas (Fig. 7b): a large dark domain, and a mosaic domain characterized by a large number of white spots. These spots are bigger than those measured on Fig. 6b, confirming thereby the increase of the crystallite size (Table 1). The large dark domain,

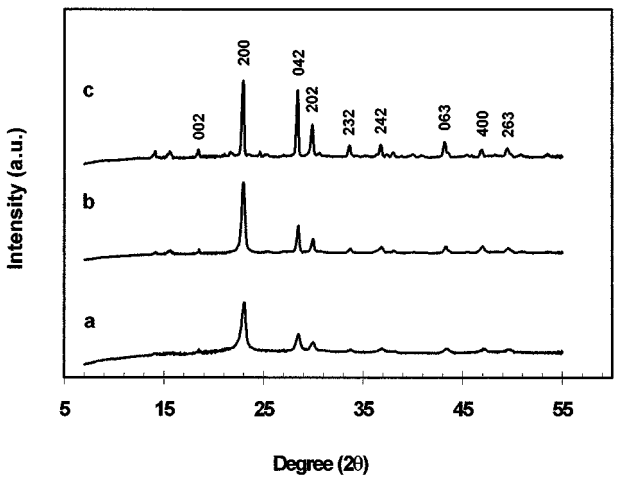

FIG. 4. Powder X-ray diffraction pattern of the three samples of $(VO)_2P_2O_7$. (a) Pyro-420; (b) Pyro-750; (c) Pyro-870.

which corresponds exactly to the individual crystallite, does not present any Bragg orientation in relation to the electron beam. The fact that the Williamson–Hall relation does not fit exactly all experimental points means that the sizes of the crystallites are polydispersed in agreement with the TEM observations, and/or that the internal strain ε is not fully isotropic. Consequently, the model of mosaic crystal, which is convenient to describe Pyro-420, is not well adapted for Pyro-750 because of its heterogeneous texture.

The XRD pattern of the partially transformed solid P420-Q (Fig. 8) shows that a mixture of $VOHPO_4 \cdot 0.5H_2O$ and $(VO)_2P_2O_7$ is obtained, as expected from the loss of weight (7.2%). No amorphous phase has been evidenced. The TEM micrographs of this mixture show that the texture of the particles is not different from that observed with Pyro-420 (Fig. 9). However, the SAED of a single platelet indicates the simultaneous presence of the two phases $VOHPO_4 \cdot 0.5H_2O$ and $(VO)_2P_2O_7$, in definite and reproducible crystallographic orientation between each other (Fig. 9):

$$[001]_{hemi} // [100]_{pyro}$$

and

$$[100]_{hemi} // [010]_{pyro}.$$

No interphase boundaries between these phases could be highlighted by TEM but the particle P420-Q seems to be composed of $VOHPO_4 \cdot 0.5H_2O$ and $(VO)_2P_2O_7$ small microdomains.

DISCUSSION

We can now summarize the essential features characterizing the textural and morphological modifications occurring during dehydration.

Whereas each bitrapezoidal platelet of $VOHPO_4 \cdot 0.5H_2O$ is a monolithic single crystal, the dehydrated pseudomorphic platelets (Pyro-420) of vanadyl pyrophosphate contain a large number of small, fairly well oriented, crystallites (mosaic particle). After dehydration at higher temperature (Pyro-750), the crystallite size Lm increases while the internal strain decreases, which indicates a textural change. The prismatic morphology of particles of vanadyl pyrophosphate is observed when the sample is calcined at 870°C (Pyro-870).

We propose a mechanism of dehydration based on these experimental observations, to account for the formation of monocrystalline mosaic particles and of prismatic particles.

Dehydration Mechanism

The mechanism of dehydration is schematized in Figs. 10a–10d to account for the formation of the observed texture up to 750°C. Steps e and f (Figs. 10e and 10f) refer to the formation of prismatic particles at higher temperature.

The dehydration reaction starts by the oriented nucleation of the vanadyl pyrophosphate phase onto the (001) plane of the precursor (Fig. 10a), as expected from the similar atomic arrangement in the $(VOHPO_4)_\infty$ sheets and in the (100) plane of $(VO)_2P_2O_7$ (26, 27). From a thermodynamic point of view, this is the most favorable situation corresponding to the lowest nucleation energy. One can propose that the reaction begins on the precursor platelet edges because of the easier escape of the water molecules situated between the layers. However, this proposal is not supported by our experiments because no interphase boundary could be evidenced in the partly transformed product (P420-Q).

During the oriented growth stage, the hemihydrate/pyrophosphate interphase boundary moves while maintaining the structural orientation relationship between the two phases. Due to the low crystallographic misfit (0.13% along $[010]_{hemi} // [001]_{pyro}$ and 11.8% along $[100]_{hemi} // [010]_{pyro}$), the existence of a coherent interface between the two phases makes the $(VO)_2P_2O_7$ nucleation easier during the further growth. The elastic strains resulting from the mismatch of the lattices are relaxed by the formation of dislocations, which move and assemble (dislocation loops) as the reaction proceeds, to form crystallite boundaries (Figs. 10b, 10c). These strains limit the pyrophosphate growth in space. However, as domains of $(VO)_2P_2O_7$ keep an orientation close to the topotactic one, they are weakly misoriented. As the interface progresses, some pyrophosphate nuclei in topotactic relation, but which cannot grow normally because of the produced strains, are still in formation. For this reason, each particle, which appears in SAED as a single crystal, is built up of a large number of small, slightly misoriented, crystallites (Fig. 10d). Both crystallite size and internal strain support the model assuming a mosaic texture

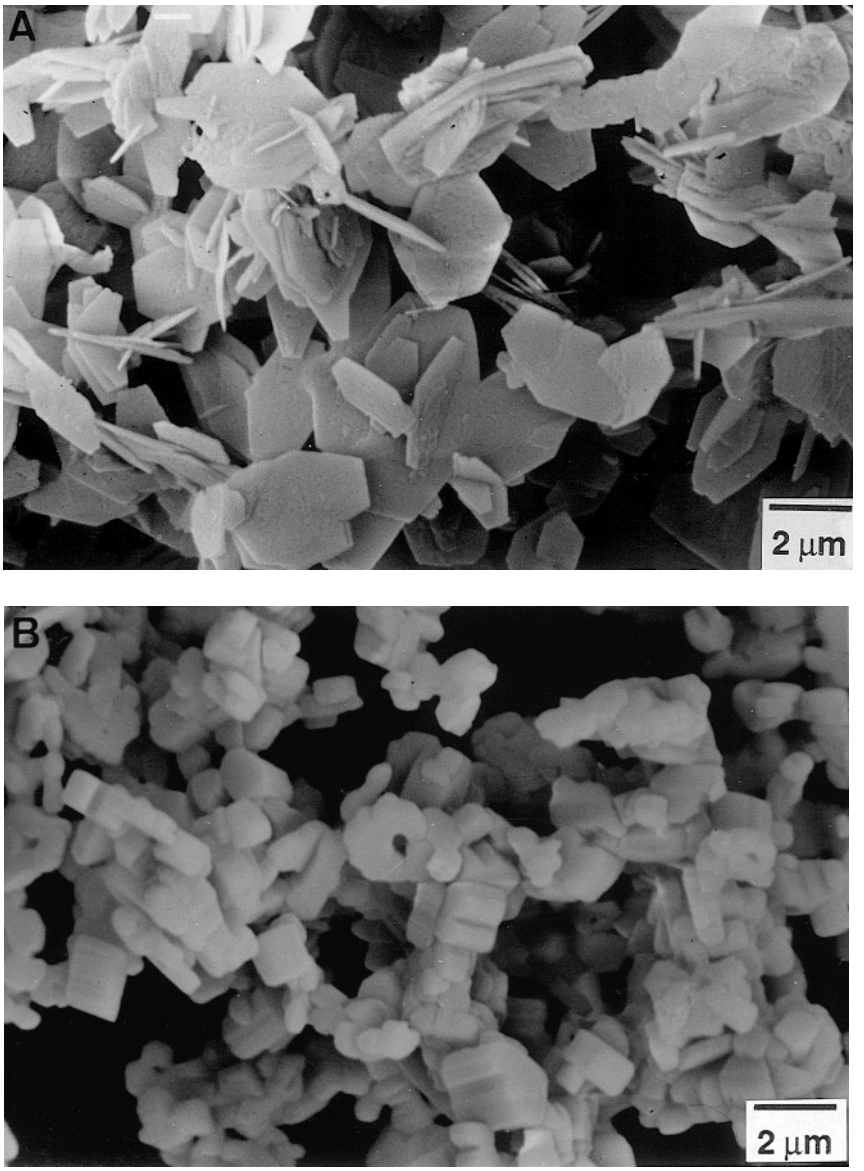

FIG. 5. SEM image of Pyro-750 (a) and Pyro-870 (b).

for each $(VO)_2P_2O_7$ particle. Indeed, the mosaic texture implies the existence of disorganized areas between each crystallite. These defects, which consist mainly of dislocations, are responsible for the slight misorientation of these crystallites. Therefore, the internal strain ε appears as a statistic measure of the inhomogeneous strains due mainly to these dislocations.

According to this reaction mechanism, the formation of a mosaic texture is a way to minimize the elastic strains produced, and, as such, is influenced by several factors. Indeed, the textural characteristics of the mother phase (shape, size and texture) and the mismatch between the lattices are decisive for the mechanism by which strains are relaxed. The number of dislocations and the rate at which they occur play also an important role in the textural modifications of the reaction product. The operating parameters (temperature, heating rate, and atmosphere) determine the kinetics of the reaction.

It is worth noting that the dehydration mechanism, though topotactic, is a reconstructive reaction: V–O, O–H, and P–O bonds are broken and a new VPO network is reconstructed. Despite the structural similarities between the hydrate and the final oxide phase, the structural elements are not *stricto sensu* maintained during the course of the dehydration reaction. In our experiments, the XRD pattern of the partially dehydrated $VOHPO_4 \cdot 0.5H_2O$ sample P420-Q shows no indication of an amorphous phase, but exhibits only the lines of the precursor and of the

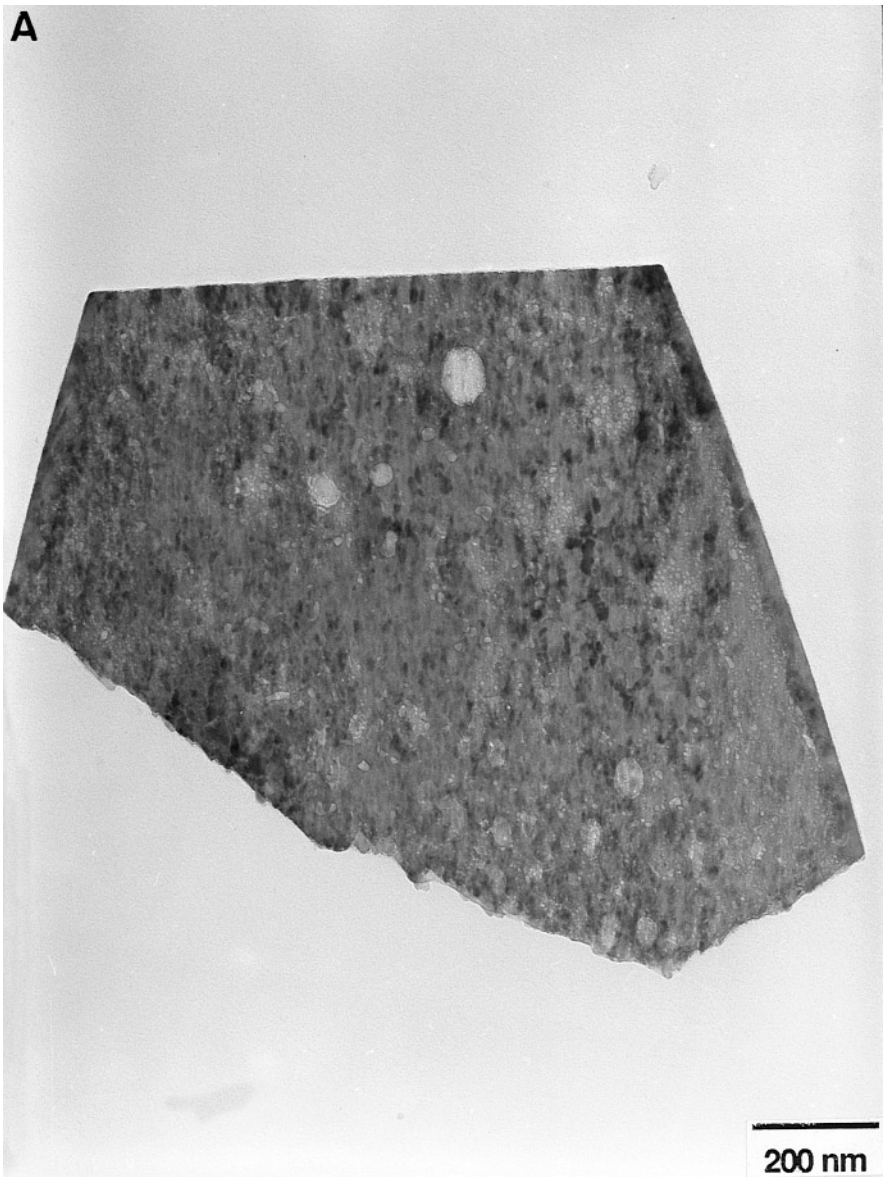

FIG. 6. (a) Bright field image of a particle of Pyro-420; (b) dark field image of the same particle and corresponding SAED showing the particle lying on the (100) plane.

final $(VO)_2P_2O_7$ solid. However, several reports suggest the formation of such an amorphous intermediate (28, 29) which can be accounted for by our model. Let us consider the stage of the reaction schematized in Figs. 10b and 10c. Particles are composed of many domains of both precursor and pyrophosphate, smaller than the initial particle. Line broadening would result from these small domains, as well as from the strains produced in this mixed particle, to such an extent that a disappearance of Bragg peaks could be expected (16). These samples being metastable, the "stabilization" of an X-ray amorphous state is strongly dependent on heat and mass transfers.

Textural and Morphology Evolution

When the temperature of calcination is higher than 420°C, the crystallinity of the material improves, owing to the usual mechanism of growth of coherent domains. Therefore, the crystallite size increases while the internal strain decreases. During a first period, the evolution of the crystallinity of $(VO)_2P_2O_7$ leads to a textural change without modification of morphology. The process begins at the center of the mosaic particle, inducing the formation of some cracks and holes (Fig. 10e). Then, the central crystallites grow before they break away the particle. This stage of

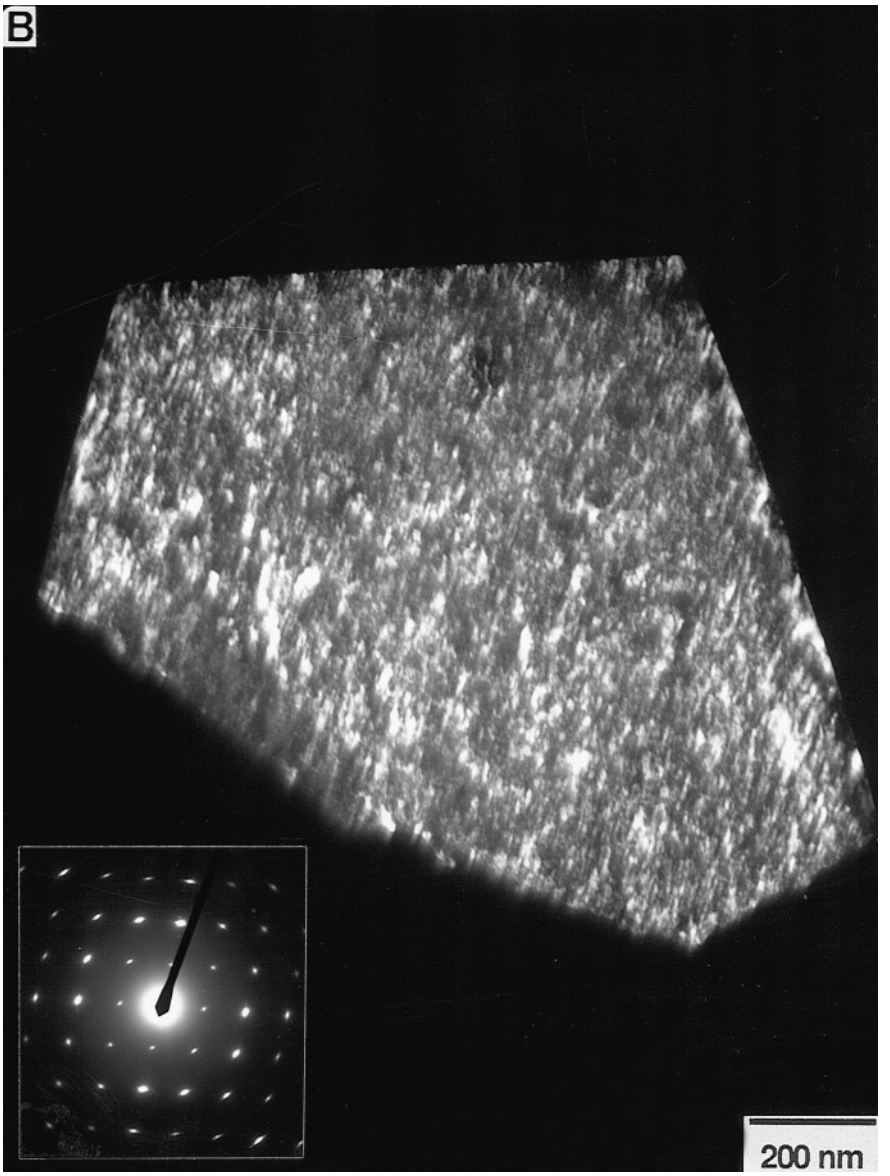

FIG. 6—*Continued*

textural evolution corresponds typically to the Pyro-750 sample. Therefore, the mosaic model becomes a less faithful representation of the real texture. The previous process spreads inside all the particle, leading to its total fragmentation in several single crystals. In the same time, the primary particles would sinter during the increase of calcination temperature to give the final prismatic morphology (Fig. 10f). This is in accordance with the TEM picture of Fig. 11, which represents a vanadyl pyrophosphate particle calcined, at 800°C for 24 h under nitrogen. Moreover, such a transformation explains the difference between the sizes of the bitrapezoidal platelets and of the final prismatic particles. It is worthwhile to note that the morphology of Pyro-870 is quite similar to the equilibrium shape of $(VO)_2P_2O_7$ crystal obtained by Curie-Wulff construction and surface energy considerations (30).

Finally, as far as defects are concerned, the vanadium oxidation state is seen to increase with the increase of internal strain, i.e., with the increase of the calcination temperature (Table 1). Such an observation is not surprising if we assume that any V^{5+} is associated with defects in the bulk of $(VO)_2P_2O_7$ (intercrystallite boundaries), rather than with a V^{5+}-containing phase, like $VOPO_4$. Nguyen *et al.* (16) have the same opinion when they modelize these defects

FIG. 7. (a) Bright field image of a particle of Pyro-750; (b) dark field image of the same particle and corresponding SAED showing the particle lying on the (100) plane.

as *bc* stacking faults which hinder the dimerization of some $(PO_4)^{3-}$ groups during dehydration process, and therefore imply the formation of V^{5+}.

CONCLUSION

The dehydration of $VOHPO_4 \cdot 0.5H_2O$ to $(VO)_2P_2O_7$ is a kind of oriented nucleation-growth, similar to the dehydration of $Ni(OH)_2$ to NiO studied by Figlarz *et al.* (31). The considerations on oriented nucleation and growth stages explain why the dehydration reaction yields $(VO)_2P_2O_7$ particles constituted by a great number of slightly misoriented, small crystallites, and also why these particles are monocrystalline. This process avoids the formation of a random texture and is responsible for the pseudomorphism. The textural modification observed when the temperature of calcination is very high explains the change of morphology into prismatic vanadyl pyrophosphate, due to fragmentation and sintering of the initial plates.

The formation of such a mosaic texture may be beneficial to catalytic performance, especially by the creation of additional surface area. Moreover, the intercrystallite boundaries, which are disorganized areas, may play a catalytic role in the selective oxidation of *n*-butane to maleic anhydride (12, 32).

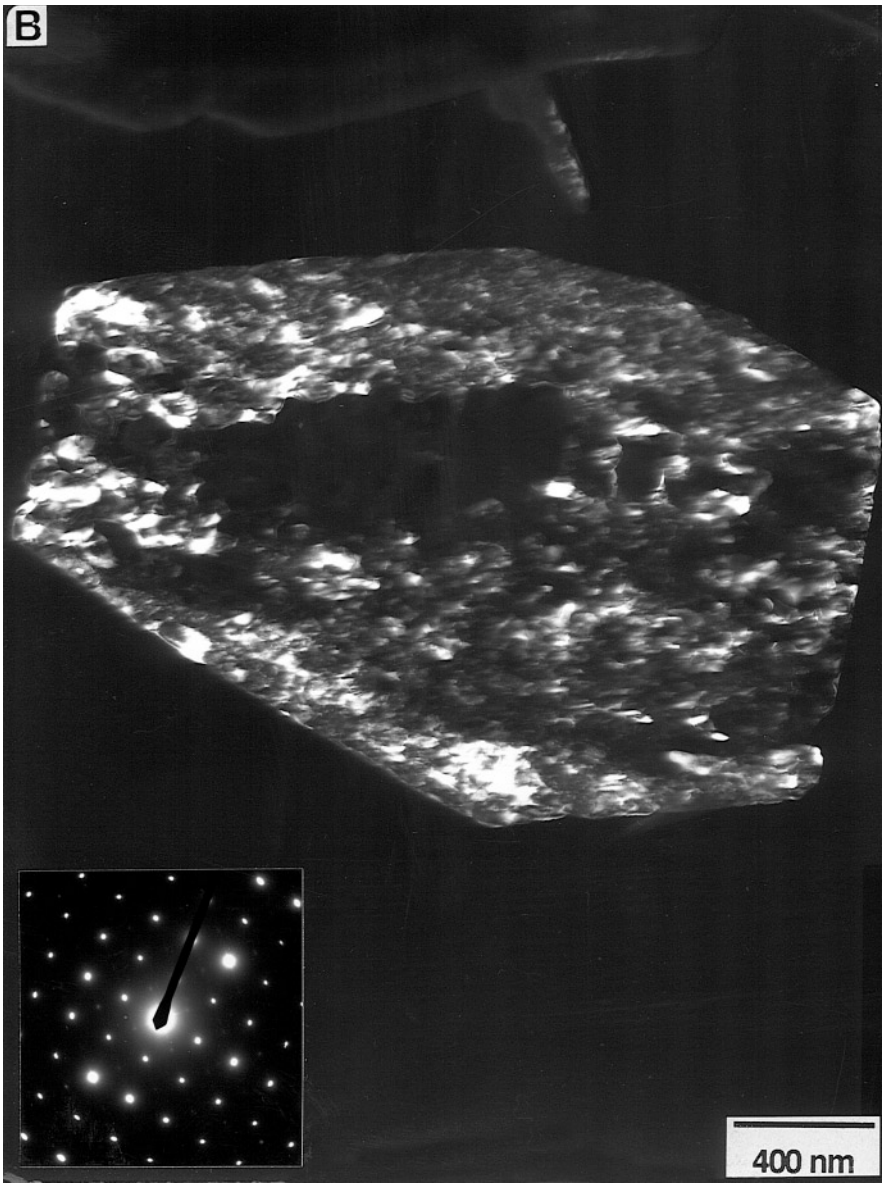

FIG. 7—*Continued*

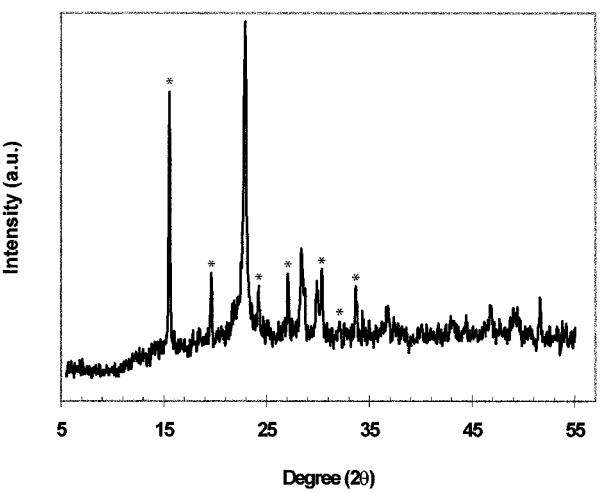

FIG. 8. Powder X-ray diffraction pattern of partially transformed $VOHPO_4 \cdot 0.5H_2O$ (P420-Q), heated at 420°C (TGA/DTA), showing the coexistence of $(VO)_2P_2O_7$ and $VOHPO_4 \cdot 0.5H_2O$ (*) lines.

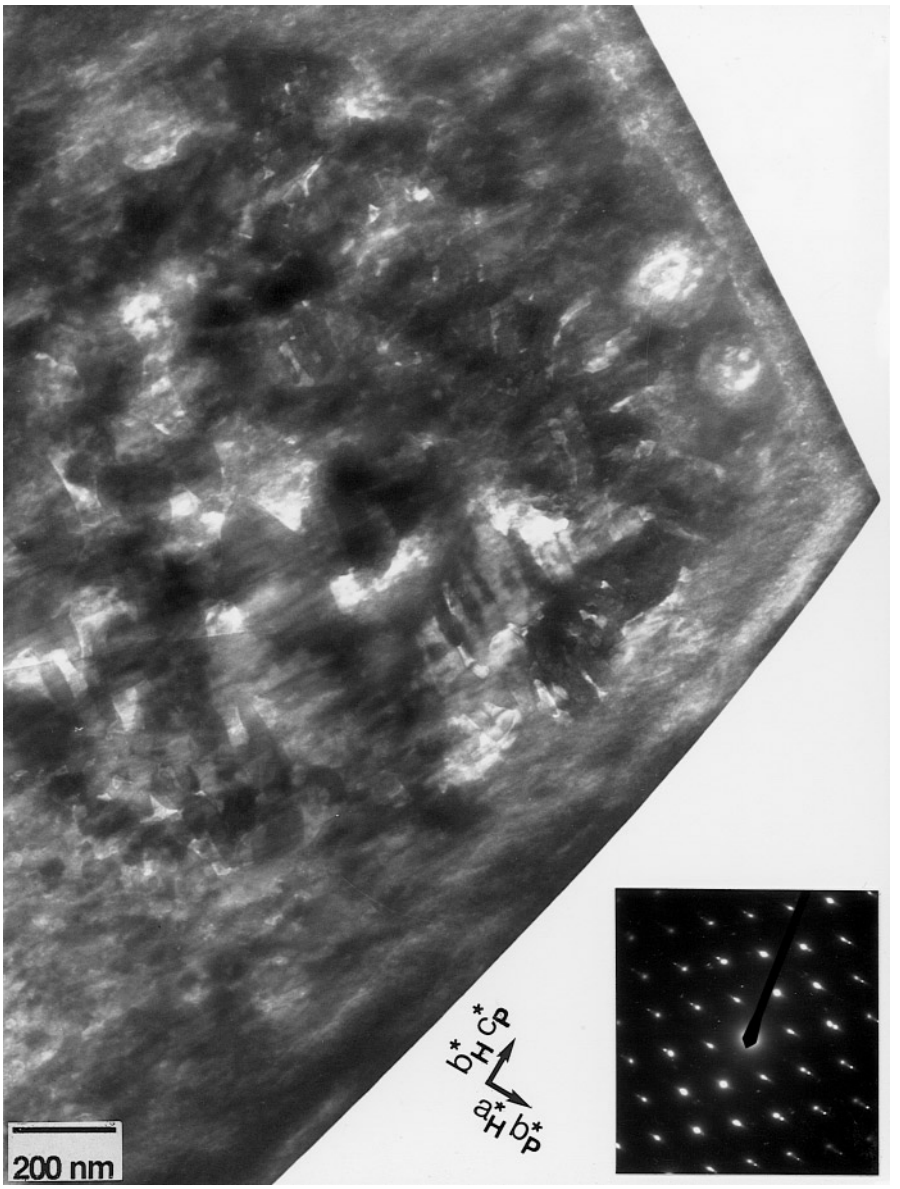

FIG. 9. Bright field image and SAED of a partially transformed $VOHPO_4 \cdot 0.5H_2O$ (P420-Q) particle, showing the structural orientation relationships between the hemihydrate (H) and $(VO)_2P_2O_7$ (P).

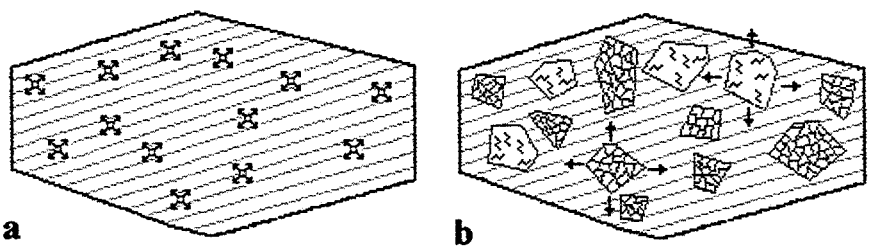

FIG. 10. Scheme of the topotactic dehydration showing textural modification (a–d) and morphology change (e–f). See text for details.

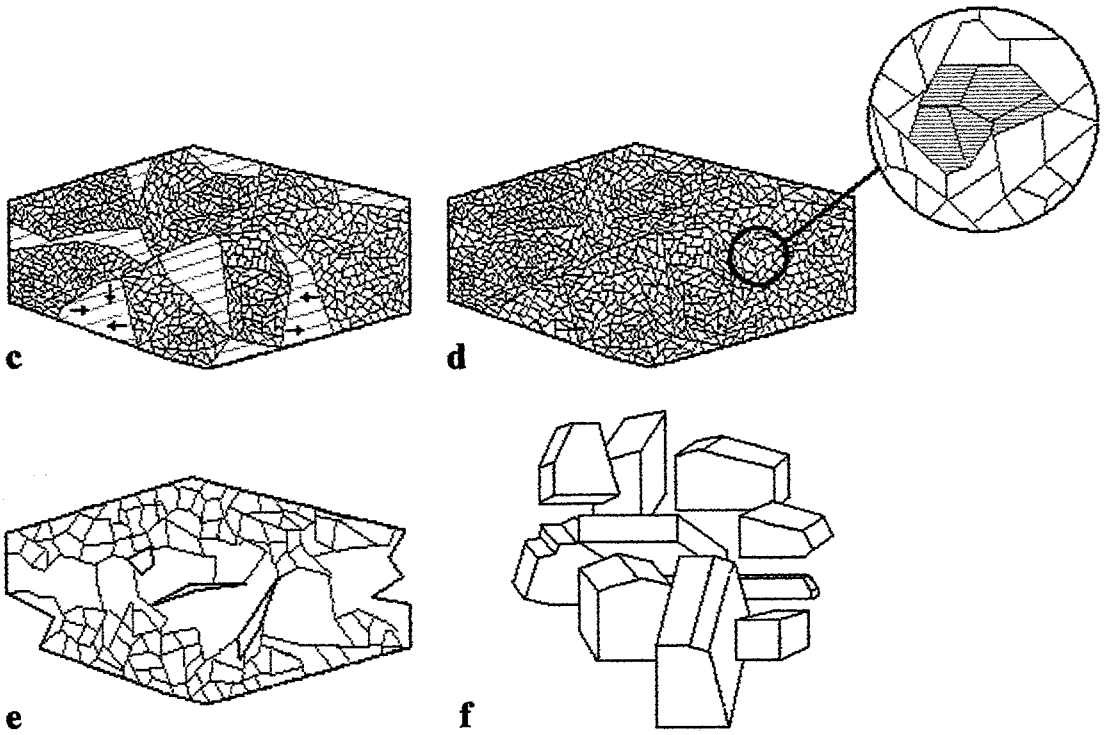

FIG. 10—*Continued*

FIG. 11. Bright field image of a precursor particle calcined at 800°C under nitrogen for 24 h.

ACKNOWLEDGMENT

Thanks are due to the Institut für Angewandte Chemie (Berlin-Adlershof) for potentiometric titrations made within the framework of the Human Capital and Mobility Program of the European Community (Contract ERBCHRXCT930290).

REFERENCES

1. International Union of Crystallography, *Acta Crystallogr. Sect. A* **33,** 681 (1977).
2. B. C. Lippens, Ph.D. Thesis, University of Delft, Netherland (1961).
3. P. P. Cord, Ph.D. Thesis, Université de Paris VI, France (1972).
4. O. Lezla, E. Bordes, P. Courtine, and G. Hecquet, *J. Catal.* **170,** 346 (1997).
5. G. Cavani and F. Trifiro, *Catalysis* **11,** 246 (1994).
6. E. Bordes, P. Courtine, and J. W. Johnson, *J. Solid State Chem.* **55,** 270 (1984).
7. C. C. Torardi and J. C. Calabrese, *Inorg. Chem.* **23,** 1308 (1984).
8. J. W. Johnson, D. C. Johnston, A. J. Jacobson, and J. F. Brody, *J. Am. Chem. Soc.* **106,** 8123 (1984).
9. H. S. Horowitz, C. M. Blackstone, A. W. Sleight, and G. Teufer, *Appl. Catal.* **38,** 193 (1988).
10. E. Kesteman, C. M. Merzouki, B. Taouk, E. Bordes, and R. Contractor, *in* "Preparation of Catalyst, VI" (G. Poncelet *et al.*, Eds.), *Stud. Surf. Sci. Catal.* **91,** 707 (1995).
11. E. Bordes and P. Courtine, *J. Chem. Soc. Chem. Commun.*, 294 (1985).
12. N. Duvauchelle, P. Courtine, and E. Bordes, to be published.
13. C. J. Kiely, A. Burrows, S. Sajip, G. J. Hutchings, M. T. Sananes, A. Tuel, and J. C. Volta, *J. Catal.* **162,** 31 (1996).
14. G. Centi, G. Golinelli, and F. Trifiro, *Appl. Catal.* **48,** 13 (1989).
15. P. T. Nguyen, A. W. Sleight, N. Roberts, and W. W. Warren, *J. Solid State Chem.* **122,** 259 (1996).
16. M. R. Thompson, A. C. Hess, J. B. Nicholas, J. C. White, J. Anchell, and J. R. Ebner, *in* "New Developments in Selective Oxidation II" (V. C. Corberan and S. V. Bellon, Eds.), p. 167. Elsevier Science, Amsterdam, 1994.
17. C. C. Torardi, Z. G. Li, H. S. Horowitz, W. Liang, and M. H. Whangbo, *J. Solid State Chem.* **119,** 349 (1995).
18. L. M. Cornaglia, C. A. Sanchez, and E. A. Lombardo, *Appl. Catal. A Gen.* **95,** 11 (1993).
19. I. J. Ellison, G. J. Hutching, M. T. Sananes, and J. C. Volta, *J. Chem. Soc. Chem. Commun.*, 1093 (1994).
20. E. Kesteman, Ph.D. Thesis, Université de Technologie de Compiègne, France (1997).
21. G. K. Williamson and W. H. Hall, *Acta Metall.* **1,** 22 (1922).
22. M. Niwa and Y. Murakami, *J. Catal.* **76,** 9 (1982).
23. C. C. Torardi and J. C. Calabrese, *Inorg. Chem.* **23,** 1308 (1984).
24. G. Busca, F. Cavani, G. Centi, and F. Trifiro, *J. Catal.* **99,** 400 (1986).
25. M. Figlarz, F. Vincent, C. Lecaille, and J. Amiel, *Powder Technol.* **1,** 121 (1967).
26. P. T. Nguyen, R. D. Hoffman, and A. W. Sleight, *Mater. Res. Bull.* **30,** 1055 (1995).
27. E. Bordes, J. W. Johnson, A. Raminosona, and P. Courtine, *in* Materials Science Monographs, Vol. 280, p. 887. Elsevier, Amsterdam, 1985.
28. J. C. Vedrine, J. M. M. Millet, and J. C. Volta, *Faraday Discuss. Chem. Soc.* **87,** 207 (1989).
29. P. Amoros, R. Ibanez, A. Beltran, D. Beltran, A. Fuertes, P. Gomes-Romero, E. Hernandez, and J. R. Carvajal, *Chem. Mater.* **3,** 407 (1991).
30. J. Ziolkowski, *Surf. Sci.* **209,** 536 (1989).
31. M. Figlarz, B. Gérand, A. Delahaye-Vidal, B. Dumont, F. Harb, A. Coucou, and F. Fievet, *Solid State Ionics* **43,** 143 (1990).
32. N. Duvauchelle, H. Zanthoff, F. Hannour and E. Bordes, *in* "Proceedings. DGMK-Conference 'C_4 Chemistry–Manufacture and Use of C_4 Hydrocarbons'" (W. Keim, B. Lücke, and J. Weitkamp, Eds.), p. 181. 1997.